JTTEE5 22:797–807
DOI: 10.1007/s11666-013-9887-x
1059-9630/$19.00 © ASM International

Fireside Corrosion Behavior of HVOF and Plasma-Sprayed Coatings in Advanced Coal/Biomass Co-Fired Power Plants

T. Hussain, T. Dudziak, N.J. Simms, and J.R. Nicholls

(Submitted October 10, 2012; in revised form December 30, 2012)

This article presents a systematic evaluation of coatings for advanced fossil fuel plants and addresses fireside corrosion in coal/biomass-derived flue gases. A selection of four candidate coatings: alloy 625, NiCr, FeCrAl and NiCrAlY were deposited onto superheaters/reheaters alloy (T91) using high-velocity oxy-fuel (HVOF) and plasma spraying. A series of laboratory-based fireside corrosion exposures were carried out on these coated samples in furnaces under controlled atmosphere for 1000 h at 650 °C. The tests were carried out using the "deposit-recoat" test method to simulate the environment that was anticipated from air-firing 20 wt.% cereal co-product mixed with a UK coal. The exposures were carried out using a deposit containing Na_2SO_4, K_2SO_4, and Fe_2O_3 to produce alkali-iron tri-sulfates, which had been identified as the principal cause of fireside corrosion on superheaters/reheaters in pulverized coal-fired power plants. The exposed samples were examined in an ESEM with EDX analysis to characterize the damage. Pre- and post-exposure dimensional metrologies were used to quantify the metal damage in terms of metal loss distributions. The thermally sprayed coatings suffered significant corrosion attack from a combination of aggressive combustion gases and deposit mixtures. In this study, all the four plasma-sprayed coatings studied performed better than the HVOF-sprayed coatings because of a lower level of porosity. NiCr was found to be the best performing coating material with a median metal loss of ~87 μm (HVOF sprayed) and ~13 μm (plasma sprayed). In general, the median metal damage for coatings had the following ranking (in the descending order: most to the least damage): NiCrAlY > alloy 625 > FeCrAl > NiCr.

Keywords air-firing, alloy 625, biomass/coal co-firing, FeCrAl, fireside corrosion, HVOF coatings, NiCr, NiCrAlY, plasma spraying, superheater corrosion, Triplex

1. Introduction

Conventional fossil fuel-fired power plants are considered to be a significant contributor to CO_2 emissions and resulting in global warming. The UK government has an ambitious target of reducing CO_2 emissions to 80% of their 1990 levels by 2050 and generating 20% of the energy from renewable sources by 2020 (Ref 1, 2). To reduce the emissions of greenhouse gases, the power generation industry is increasingly moving toward higher steam temperatures, hence higher efficiencies, and using more *carbon-neutral* biomass in the fuel mix. However, the heat exchangers (superheaters/reheaters) in the power plants may encounter very aggressive fireside corrosion at higher steam operating temperatures coupled with biomass-derived flue gases.

Fireside corrosion is an on-going concern for the power generation industry where coal is being used as fuel (Ref 3). Fireside corrosion is defined as the loss of heat exchanger material due to chemical reactions with the combustion gases and deposits at high temperatures (Ref 4-6). Fireside corrosion is the single most reason for tube failures in pulverized fuel-fired power plants (Ref 3, 5-7). These failures are difficult to repair and result in unscheduled plant-downtime. Since the introduction of biomass, the issue of fireside corrosion has become more significant (Ref 8-10). High corrosion-resistant overlay coatings have the potential to provide suitable protection to boiler steels from the aggressive fireside corrosion. Development of effective corrosion resistance coatings will enable the power plants to operate at higher steam temperatures (and pressures) and also utilize lower grades of fuel. Thermal spray coatings can provide suitable protection to the underlying substrate by selective oxidation of chromium or aluminum to produce a protective oxide layer at high temperatures (Ref 11). Thermal spray coatings can be applied to both newly built power plants and retrofit applications.

High-velocity oxy-fuel (HVOF) spraying and plasma spraying are the two most widely used thermal spraying techniques, which have found many applications in high-temperature oxidation/corrosion (Ref 11-14). In the

T. Hussain, T. Dudziak, NJ. Simms, and **JR. Nicholls**, Centre for Energy and Resource Technology, Cranfield University, Bedfordshire MK43 0AL, UK. Contact e-mail: t.hussain@cranfield.ac.uk.

Table 1 Nominal compositions (wt.%) of the coatings used in fireside corrosion exposures

	Al	C	Co	Cr	Cu	Fe	Mo	Nb + Ta	Si	Y	N	O	Mn	P	S	Ni
NiCrMo (Nb + Ta)/alloy 625	0.2		0.1	21.3	0.18	0.1	8.9	3.58	0.13		0.03					Bal.
NiCr		0.1		46.0		1.1			2.1			0.03				Bal.
FeCrAl	5.9	0.03		21.7		Bal.			0.83				0.76	0.01	0.01	
NiCrAlY	9.9			22.0						0.9		0.02				Bal.

HVOF process, a fuel (gas/liquid) and oxygen are mixed and combusted in the combustion chamber. The powder particles typically attain velocities in the range of 600-1000 m/s while reaching temperatures which allow them to be in a molten or semi-molten state before impact (typical gas temperature of ~3100 °C) (Ref 14-16). In comparison with plasma spraying, in HVOF spraying, the powder particle temperatures are relatively low, whereas particle velocities are relatively high (Ref 17). In plasma spraying, an inert gas (typically argon) is superheated by a dc arc or a radio frequency discharge. The powder particles are melted by the immense heat of the plasma (~16,000 °C) and typically attain velocities of ~120-600 m/s (Ref 14, 16).

In this study, coatings were prepared from alloy 625, NiCr, FeCrAl, and NiCrAlY onto a T91 steel substrate using HVOF and plasma spraying. Fireside corrosion behavior of these coatings was examined in detail. The test conditions were targeted at simulating the environments on the surfaces of the superheaters/reheaters in a pulverized fuel boiler firing a mixture of a coal (UK Daw Mill) and a biomass (cereal co-product, CCP) mixed at 80:20 wt.%. The coatings were tested according to the well-established deposit-recoat test method at 650 °C for 1000 h. After the exposure, the samples were cross-sectioned and examined in an ESEM with EDX mapping. Dimensional metrology was used as the primary route for quantifying the metal damage.

2. Experimental Methods

2.1 Sample Preparations

Commercially available ferritic steel T91 (0.07-0.14 C, 0.2-0.5 Si, 0.3-0.6 Mn, 8.0-9.5 Cr, 0.85-1.05 Mo, 0.18-0.25 V, 0.03-0.07 N, 0.06-0.1 Nb, ≤ 0.4 Ni wt.%) was chosen as a substrate material for this study. The alloy was sourced in the form of conventional boiler tubes with 38-mm outer diameter. Four commercially available powders: alloy 625, NiCr, FeCrAl and NiCrAlY were manufactured by Sulzer Metco Inc. (USA) and sprayed onto T91 using HVOF and plasma spraying at Sulzer Metco Inc. (USA). Nominal compositions of the powders are given in Table 1. The size range of the powders used in this study was 15 ± 45 μm. The substrates were degreased and grit blasted before coating deposition.

Table 2 shows the spraying parameters for all four coatings using a HVOF spraying system. HVOF coatings were sprayed with a Sulzer Metco Diamond Jet® DJ9A gun using a standard nozzle with propylene as a fuel gas.

Table 2 Spraying parameters for HVOF-sprayed coatings

	Alloy 625	NiCr	FeCrAl	NiCrAlY
Fuel gas	Propylene	Propylene	Propylene	Propylene
O_2 flow rate, nlpm	310	316	316	316
Fuel gas flow rate, nlpm	70	65	79	65
Air flow rate, nlpm	345	270	345	270
Powder feed rate, g/min	60	45	38	45
Stand off distance, mm	230	230	230	230
Scanning rate, ft/min	200	200	200	200

nlpm = normal litre per minute

Table 3 Spraying parameters for plasma-sprayed coatings

Parameter	Alloy 625	NiCr	FeCrAl	NiCrAlY
Primary gas (Ar) flow, slpm	125	100	70	100
Secondary gas (He) flow, slpm	200	200	70	200
Current, A	450	550	550	550
Voltage reading, V	186	168	131	169
Powder feed rate, g/min	75	75	75	75
Stand off distance, mm	130	130	130	130
Scanning rate, ft/min	500	500	500	500

slpm = standard litre per minute

Table 4 Nominal gas compositions used in fireside corrosion tests

	N_2, vol.%	O_2, vol.%	CO_2, vol.%	H_2O, vol.%	SO_2, vppm	HCl, vppm
Air-firing	73.8	4	14	8	1300	400

Table 5 Deposit compositions (mol.%) used in fireside corrosion tests

Deposit	Na_2SO_4	K_2SO_4	Fe_2O_3
D1	37.5	37.5	25

The stand-off distance for all spray runs was fixed at 230 mm, and the scanning rate was set at 200 ft/min. The gun was air cooled during the spray deposition. Table 3 shows the spraying parameters for the plasma-sprayed coatings. A Sulzer Metco Triplex plasma spray gun with argon as a primary gas and helium as a secondary gas were used for the coating deposition. The stand-off distance for all the four coatings was 130 mm and a scanning speed was

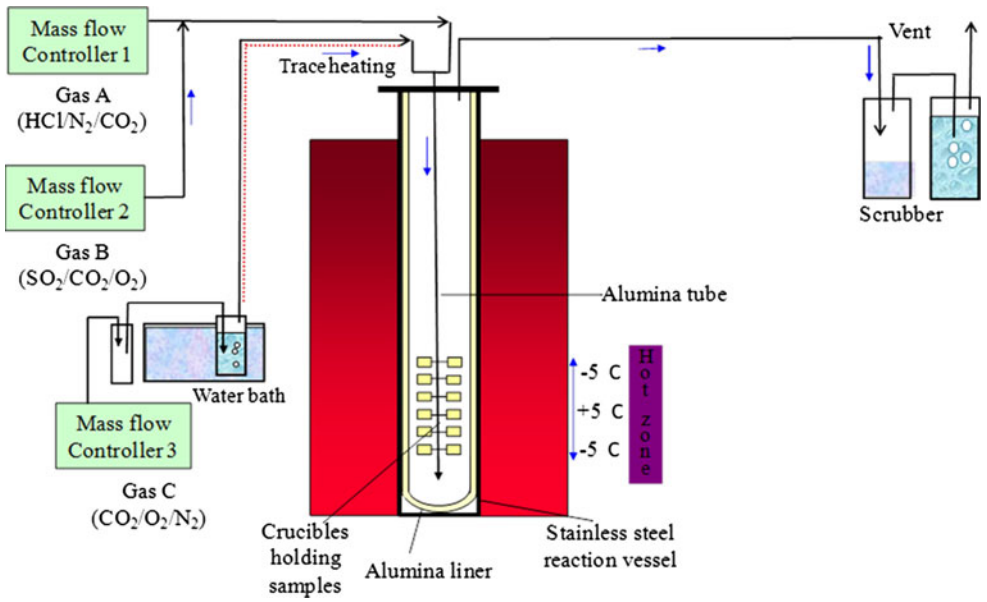

Fig. 1 Schematic diagram of a controlled atmosphere furnace setup for fireside corrosion in simulated air-firing combustion gases

500 ft/min. In all cases, optimized spraying parameters, which were developed for commercial applications by Sulzer Metco Inc., were used to produce the coatings for this study. Following coating deposition the coated tubes were cut and machined into tube segments with dimensions of ~15 mm chord, 15 mm long and 5-mm wall thickness for fireside corrosion tests.

2.2 Fireside Corrosion Exposure Conditions

The coated samples were tested in simulated air-fired combustion gases which were derived from the combustion of a typical UK coal (Daw Mill) mixed with a biomass (CCP) at 80:20 wt.%. The compositions of the fuels are available in Ref 10. The combustion gases produced by these fuels have been calculated using models that have been validated by pilot/plant scale experiments, and the gas compositions have been simplified to their key active components for the fireside corrosion tests (Ref 5, 18). The nominal composition of the gas used in this study is given in Table 4. The samples were exposed in the combustion gases at 650 °C. The test was run for 1000 h using well-established deposit-recoat test methods, which were developed for high-temperature corrosion tests (Ref 19-21). The coated samples were cleaned before exposure using volasil (degreaser) followed by isopropanol in an ultrasonic bath for 20 min. The cleaned samples were painted using an artist's paint brush to apply a deposit loading of 20 mg/cm^2. Table 5 shows the chemical composition of the deposit, referred to as D1, used in this study. This is a widely used standard deposit for screening tests as it represents a composition of alkali-iron tri-sulfate that has been identified as being the principal cause of fireside corrosion in superheaters/reheaters in pulverized coal-fired power stations (Ref 3, 4, 7, 22, 23). The deposit was mixed with isopropanol to form thick slurries for painting onto the specimens. The test was cycled every 200 h and repainted with deposits to replenish any salts, resulting in a deposition flux of ~100 μm/cm^2·h. The progress of the samples was monitored using conventional mass change measurements every 200 h. The samples were weighed with/without crucibles as well as before and after applying the deposits.

2.3 Experimental Setup

The tests were carried out in an alumina-lined vertical-controlled atmosphere furnace. The furnace assembly can hold up to 24 test samples at one time in individual alumina crucibles in the hot zone. The temperature of the hot zone was within ±5 °C of the set point. A schematic diagram of the controller atmosphere fireside corrosion test is shown in Fig. 1. To achieve the required environment, premixed gases were supplied to the furnace through mass flow controllers. A mixed gas containing CO_2, O_2, and N_2 was passed through a de-ionized water bubbler, which was kept at 40 °C in a water bath to add the required amount of moisture to the gas stream before mixing with the corrosive gas species (HCl, SO_2, etc.). The exhaust gas from the controlled atmosphere furnace passed through an initially empty bottle to trap the condensate and then through a NaOH scrubber solution before finally being vented into the atmosphere.

2.4 Pre- and Post-exposure Measurements

Dimensional metrologies of the samples before and after the exposure in the corrosion tests form a key part of this research. The dimensions of each of the samples were measured using a digital micrometer (with a resolution of 1 μm) before their exposure. Post-exposure metrology on sample's cross sections was carried out using an image analyzer connected to an optical microscope with a

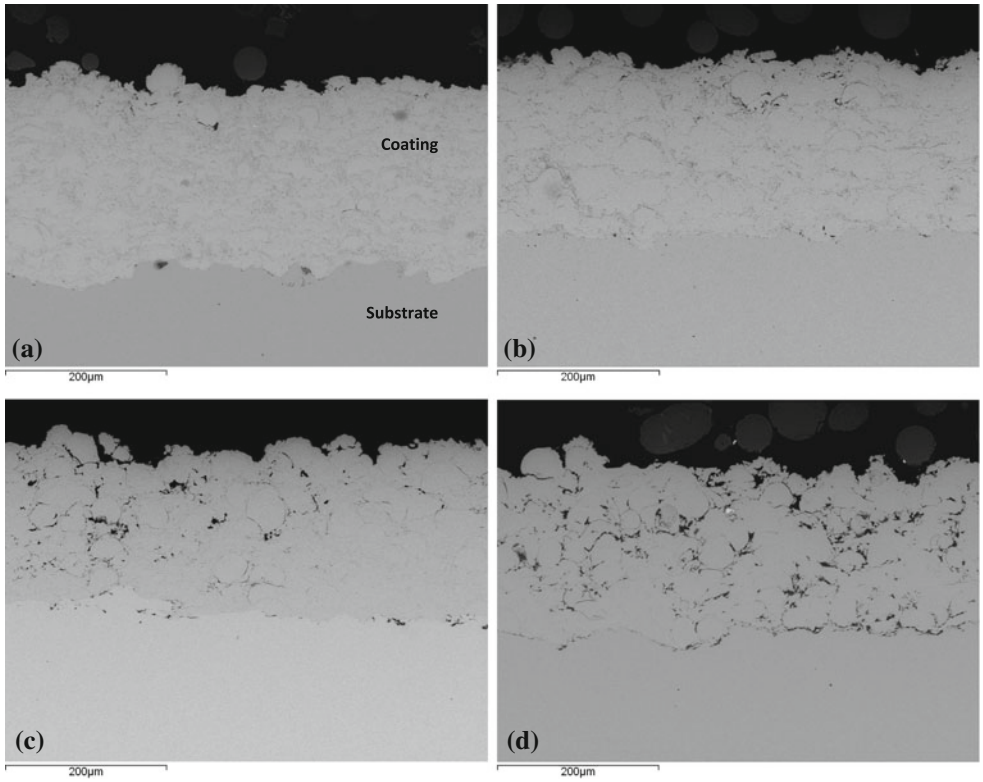

Fig. 2 BSE images of the HVOF-sprayed (a) alloy 625, (b) NiCr, (c) FeCrAl, and (d) NiCrAlY coatings on T91 substrate

motorized *x-y* co-ordinate table, to determine the remaining metal thickness and any internal damage. Reference samples were also prepared to measure the systematic and random variation in the measurements. The post-exposure co-ordinates from the image analyzer were transferred into spread sheets and compared with the pre-exposure measurements to determine a metal loss distribution for each sample. The metal loss distributions were further processed to generate cumulative probability plots. A detailed description of the method has been published in Ref 10, 24.

The exposed samples were vacuum impregnated using a low shrinkage cold-mounting resin-filled with ballotini (to further reduce shrinkage) in a specially designed jig. The samples were then cross-sectioned, ground, and polished to a 1-μm diamond grit finish using non-aqueous lubricant, to avoid dissolving water-soluble corrosion products. The samples were investigated in back-scattered electron (BSE) imaging mode in an environmental scanning electron microscope (ESEM) (FEI, Eindhoven, the Netherlands). An Oxford Instruments ISIS Link (ISIS) system attached to the ESEM was used to identify the elemental compositions on the cross sections. EDX mapping was also used to identify the elemental distribution of key components across the coating/scale interfaces. To quantify the porosity of the coatings, image analysis software (ImageJ, the U.S. National Institute of Health, MD) was used. Five representative BSE images (at 1000× magnification) of each coating were selected for measurement; each image had a field of view of approximately 120 × 90 μm. Threshold function in the image analysis software was used to measure the porosity.

Table 6 Measurements of coating porosity with standard error in the mean (all measurements were taken on BSE images with a field size of 120 × 90 μm)

Coatings	HVOF sprayed	Plasma sprayed
Alloy 625	1.7 ± 0.2	0.9 ± 0.1
NiCr	2.1 ± 0.4	0.9 ± 0.2
FeCrAl	4.3 ± 0.7	3.5 ± 0.5
NiCrAlY	3.5 ± 0.6	0.8 ± 0.1

3. Results and Discussions

3.1 As-Sprayed Coating Microstructure

Figure 2 shows the HVOF-sprayed microstructure of alloy 625, NiCr, FeCrAl, and NiCrAlY coatings on T91 substrate. Typically, the HVOF-sprayed coatings were ~220-230 μm thick. The microstructures of alloy 625 and NiCr coatings showed little porosity and well-bonded coating-substrate interface. The microstructures of the FeCrAl and NiCrAlY coatings showed interparticle porosity and partially melted particles. The porosities of the coatings were measured using image analysis, and the averages along with the standard errors of the means are

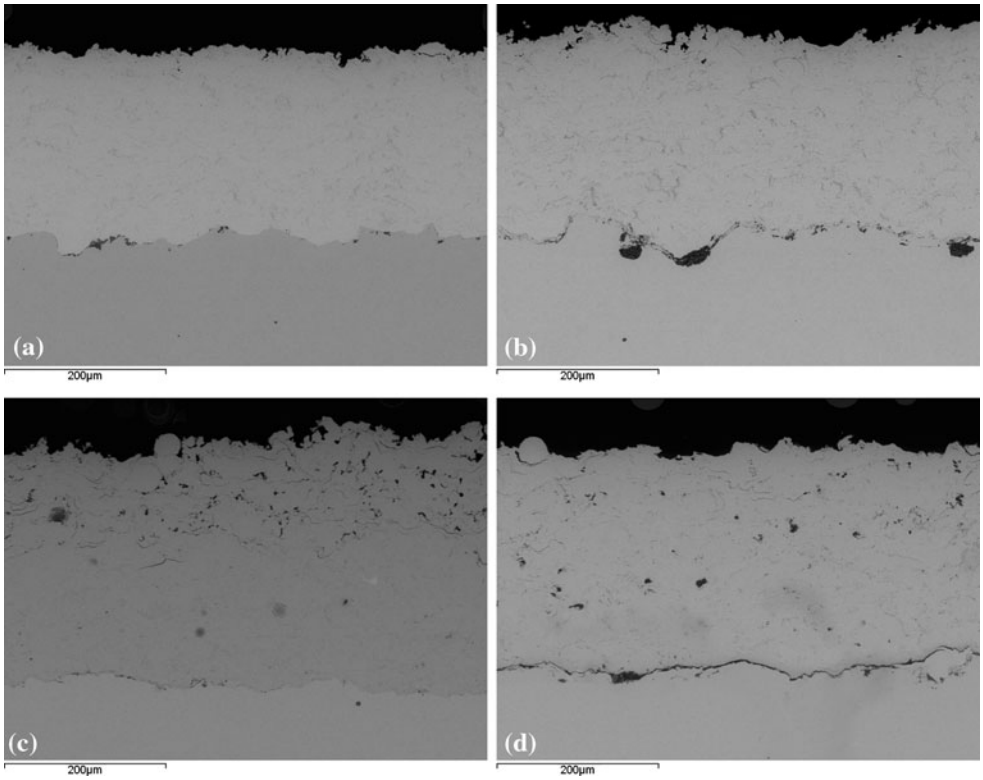

Fig. 3 BSE images of the plasma-sprayed (a) alloy 625, (b) NiCr, (c) FeCrAl, and (d) NiCrAlY coatings on T91 substrate

shown in Table 6. FeCrAl and NiCrAlY coatings were more porous than alloy 625 and NiCr coatings, taking the standard error of mean into account. The darker contrast particles along to coating-substrate interface were identified as alumina grits from the grit-blasting surface preparation.

The cross sections of the plasma-sprayed alloy 625, NiCr, FeCrAl, and NiCrAlY coatings on T91 substrates are shown in Fig. 3. Typically, the coatings were ~220-270 μm thick. The microstructures of plasma-sprayed coatings showed good interparticle interface and much less porosity. However, the cross section of NiCrAlY coating showed the presence of a hairline crack at the coating-substrate interface. The porosity levels of plasma-sprayed alloy 625, NiCr and NiCrAlY coatings were less than 1% (Table 6). FeCrAl coating had the highest level of porosity, and the microstructure also showed a top 50-μm porous layer, which could be due to spraying instabilities in the final pass. The porosity of all four plasma-sprayed coatings was less than HVOF-sprayed coatings produced from the same powders. Typically, the plasma-sprayed coatings have porosity levels of 2-5 vol.%, and HVOF-sprayed coatings have porosity levels of 0.1-2 vol.% (Ref 16). It should be noted that the measurement of porosity is sensitive to the sample preparation and the measurement technique (Ref 25). Higuera et al. (Ref 26) reported 1 vol.% porosity for a plasma-sprayed NiCr coating and 0.7 vol.% porosity when the same powder was sprayed using HVOF equipment. Azarmi et al. (Ref 27) reported a porosity of ~2.5% for an alloy 625 coating which was plasma sprayed using optimized parameters, and Yuan et al. (Ref 28) reported a porosity of 3.2% for a HVOF-sprayed NiCrAlY coating. These porosity values are within the range reported in this article. Although it is considered that the HVOF spraying produces less porous coatings than conventional plasma spraying, the advances in plasma-spraying technology and the utilization of the optimized process parameters resulted in lower porosity in the case of plasma-sprayed coatings in this study.

3.2 Measurement of Metal Damage

The outputs of the dimensional metrology provide the best measurements of the corrosion performance of the different materials (Ref 8, 18-21, 29), as they give a distribution of metal damage data for each exposed sample. According to the draft standards, available for high-temperature corrosion assessments (Ref 19-21), the results are plotted as change in metal as a function of cumulative probability. Analysis of corrosion data using standard statistical methods is becoming more widespread as the test methods are standardized.

Figure 4(a) shows the change in metal distribution plotted against cumulative probability for HVOF-sprayed alloy 625, NiCr, FeCrAl, and NiCrAlY coatings exposed with a deposit (D1) to the simulated air-fired combustion gases at 650 °C for 1000 h. Cross section of each sample was measured using an image analysis system to provide ~17-20 metal loss measurements which were then ordered

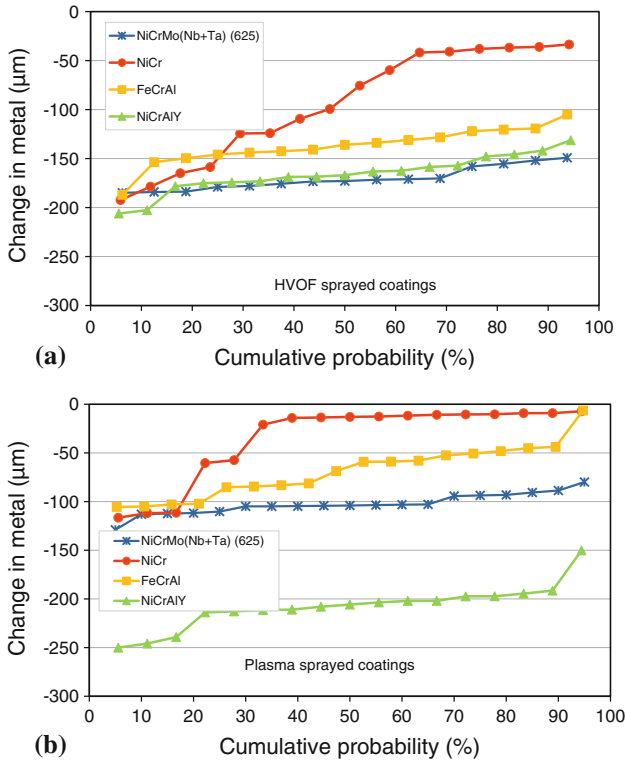

Fig. 4 Changes in metal thickness vs. cumulative probability of HVOF- and plasma-sprayed alloy 625, NiCr, FeCrAl, and NiCrAlY coatings covered with deposits in simulated air-fired combustion gases after 1000 h at 650 °C

to allow the extent of the attack to be determined. The data for HVOF-sprayed NiCr coating showed that the median metal loss (50% cumulative probability) was ~87 μm, which means that 50% of the sample surface had suffered a metal loss of more than 87 μm. Similarly, 65% of the sample surface of the NiCr coating had suffered a metal loss of more than ~40 μm. FeCrAl coating suffered more corrosion damage than the NiCr coating. The plot illustrates that all the measured points on FeCrAl sample surface suffered a corrosion damage of 100 μm or more over the duration of 1000 h in the test condition. The regions of the cumulative probability plots that are effectively flat correspond to an even metal loss, and a gradient indicates that the sample has suffered damage of various depths. It is interesting to notice that both alloy 625 and NiCrAlY coatings suffered a similar degree of corrosion damage.

Figure 4(b) shows the change in metal versus cumulative probability for plasma-sprayed alloy 625, NiCr, FeCrAl, and NiCrAlY coatings exposed with deposits in simulated combustion gases at 650 °C for 1000 h. Plasma-sprayed alloy 625, NiCr, and FeCrAl coatings showed much better corrosion performance compared to those of their HVOF counterparts. However, plasma-sprayed NiCrAlY coating suffered a corrosion damage of more than 200 μm on 90% of the sample surface, and 18% of the sample surface suffered damage levels of more than 250 μm (the initial coating thickness was ~250 μm). The crack present in the as-sprayed coating-substrate interface (Fig. 3d) could contribute to this loss. Plasma-sprayed NiCr coating had a median metal damage of 13 μm, which is significantly lower than the HVOF-sprayed NiCr coating. Only 17% of the sample surface suffered from a corrosion damage of more than 115 μm. Unlike the HVOF-sprayed alloy 625 and NiCrAlY coatings, there was a clear distinction between the performances of plasma-sprayed alloy 625 and NiCrAlY coatings; alloy 625 performed better than NiCrAlY. Median metal loss value of plasma-sprayed alloy 625 was 110 μm, as opposed to 170 μm for HVOF-sprayed alloy 625 coating.

A traditional target for fireside corrosion rate values for superheaters/reheaters in conventional power plants is ~40-50 μm/1000 h. All the coatings tested in this study exceeded this limit by a large amount, except plasma-sprayed NiCr. However, it should be noted that D1 is an aggressive deposit, which has traditionally been used for accelerated corrosion tests for screening purposes. To put into a clear perspective, a bare T91 substrate without any coating has a median metal loss of ~625 μm covered in deposit D1 in simulated air-fired combustion gases at 650 °C for 1000 h.

3.3 Post-Exposure Coating Microstructure

3.3.1 HVOF-Sprayed Coatings. Cross-sectional images of the HVOF coatings along with the EDX elemental maps after exposure in the simulated combustion gases at 650 °C are shown in Fig. 5. Following the corrosion tests, only a thin layer of alloy 625 coating was left on the substrate, and the scale was composed of chromium oxide. A band of sulfur was present underneath the scale, on the coating surface, indicating degradation of the coating by a sulfidation mechanism. The cross-sectional image of the HVOF-sprayed NiCr (Fig. 5b) coating clearly shows the interparticle boundaries and a pitting-type attack of the coating. Similar to alloy 625 coating, a chromium-rich oxide layer was detected at the coating-mixed deposit/corrosion product boundary, and sulfur was detected beneath this chromium oxide layer. The role of sulfur in the corrosion mechanism can be confirmed by the detection of this sulfur-rich layer. Both sodium and potassium from the applied deposits were found in increasing concentrations toward the mixed deposit/corrosion product layer.

Figure 5(c) shows the cross section and corresponding elemental maps of HVOF-sprayed FeCrAl coating after the corrosion test. The cross-sectional image showed only ~100 μm of coating left on the T91 substrate. The particle boundaries and the morphologies of partially melted particles can be clearly identified. Elemental mapping showed that aluminum was enriched at the coating-mixed deposit/corrosion product interface and coating-substrate interface. A thick layer of chromium oxide was formed at the coating-mixed deposit/corrosion product boundary; however, similar to alloy 625 and NiCr coatings, a layer of sulfur was present underneath this chromium oxide layer. The cross-sectional micrograph of NiCrAlY coating showed the most severe damage following the exposure in the corrosion test. Only a very thin layer of coating was

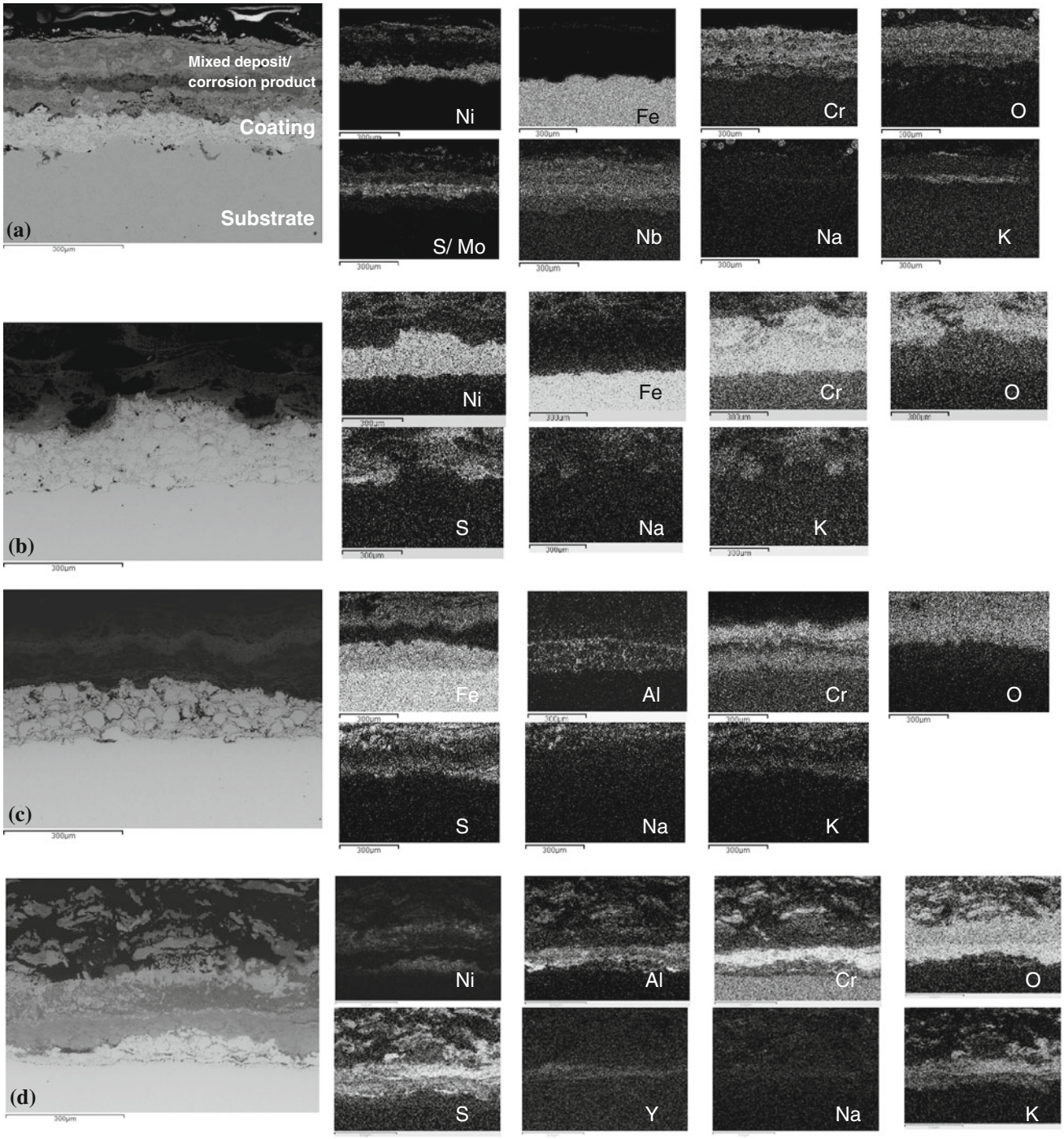

Fig. 5 BSE images and EDX maps showing the HVOF-sprayed (a) alloy 625, (b) NiCr, (c) FeCrAl, and (d) NiCrAlY coatings covered with deposits in simulated air-fired combustion gases after 1000 h at 650 °C

left on the T91 substrate. The inner layer of the mixed deposit/corrosion product was composed of aluminum, chromium, and oxygen, and the outer layer was composed of nickel, oxygen, and sulfur. In the presence of alkali salts and sulfur-rich environment, nickel was consumed through formation of nickel sulfate (Ref 30). In the outer layer, large quantity of potassium was also detected. NiCrAlY coating contained the highest amount of aluminum out of all four coatings (9 wt.%); however, the temperature was not sufficiency high enough to produce a protective alpha-alumina layer.

3.3.2 Plasma-Sprayed Coatings. Figure 6 shows the cross-sectional images of the plasma-sprayed coatings along with the EDX elemental maps after exposure in simulated combustion gases at 650 °C for 1000 h. The BSE cross-sectional image in Fig. 6(a) shows ~150 μm of alloy 625

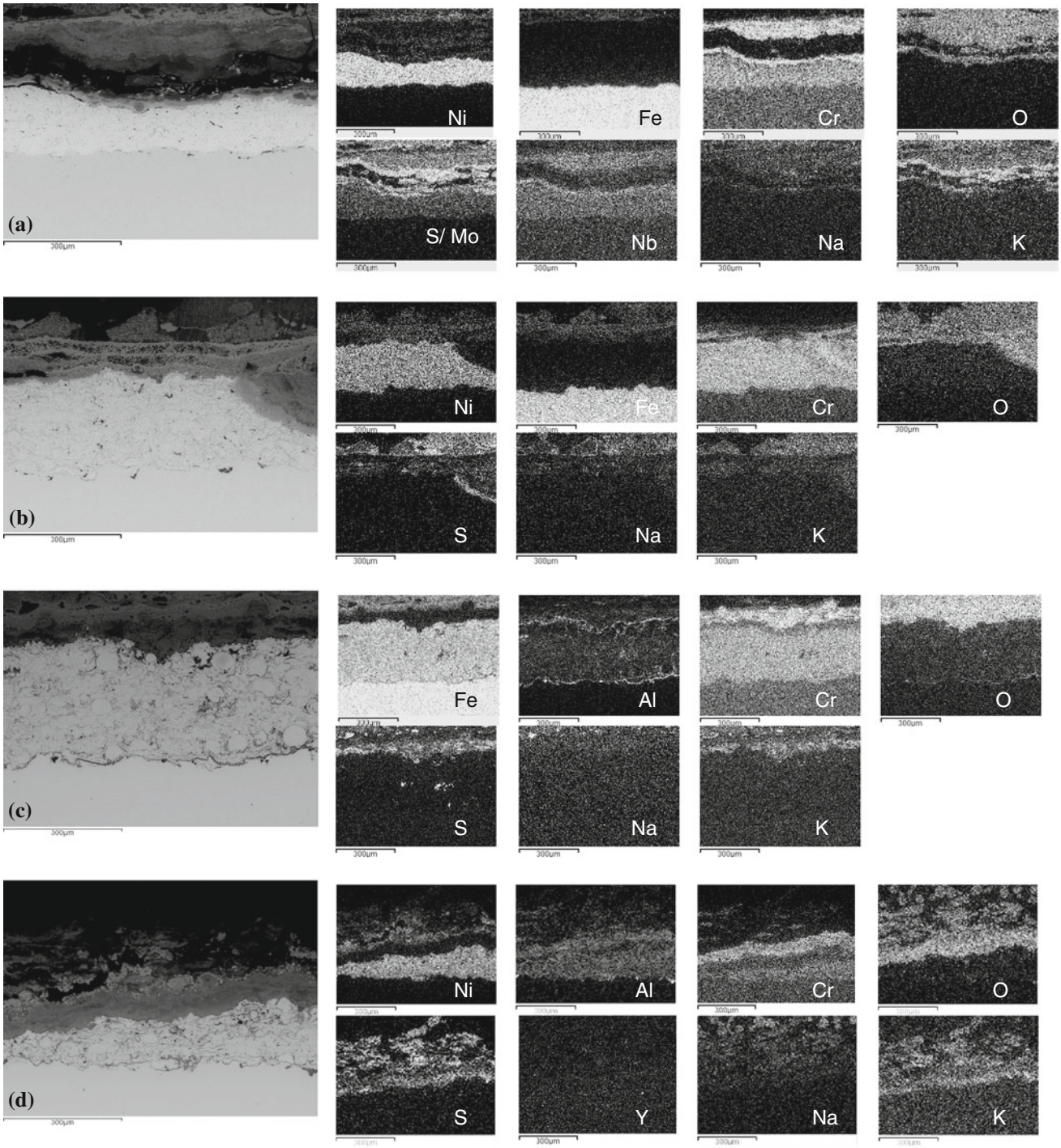

Fig. 6 BSE images and EDX maps showing the plasma-sprayed (a) alloy 625, (b) NiCr, (c) FeCrAl, and (d) NiCrAlY coatings covered with deposits in simulated air-fired combustion gases after 1000 h at 650 °C

coating on the T91 substrate, which is significantly more than the thickness of the HVOF-sprayed alloy 625 coating after the test (Fig. 5a). The plasma-sprayed alloy 625 coating has a chromium- and oxygen-rich inner scale (chromium oxide), above which a layer rich in sulfur was present. In the outer scale, nickel, chromium, oxygen, and sulfur were present (a mixture of nickel sulfate and chromium oxide). Figure 6(b) shows the cross section through a plasma-sprayed NiCr coating after the test. The micrograph shows ~235-μm-thick coating with a pitting-type attack. The corrosion front at the pit was rich in sulfur, which plays a key role in the fireside corrosion. The gaseous environment at the exposure temperature generated sufficient SO_3 to stabilize the molten alkali-iron tri-sulfate in the deposit

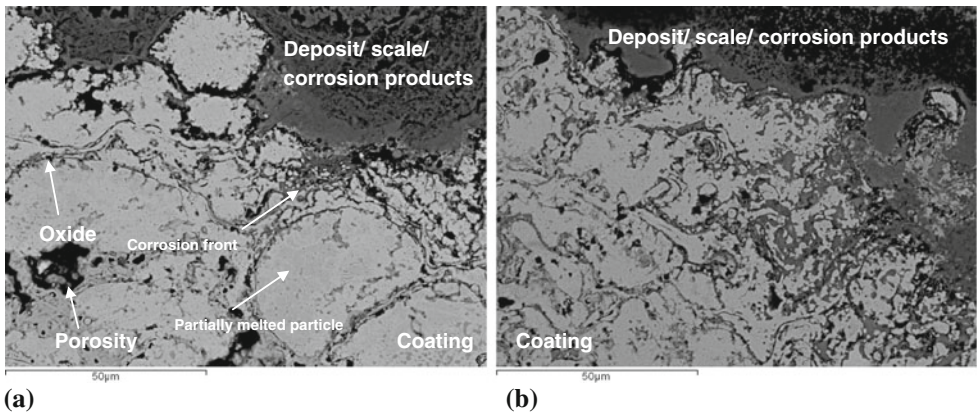

Fig. 7 High magnification BSE images of the top section of (a) HVOF and (b) plasma-sprayed NiCr coatings covered with deposits in simulated air-fired combustion gases after 1000 h at 650 °C

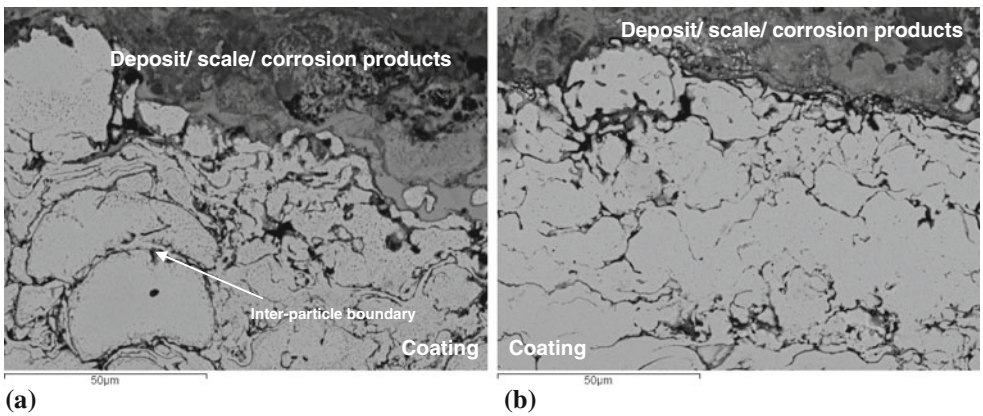

Fig. 8 High magnification BSE images of the top section of (a) HVOF and (b) plasma-sprayed FeCrAl coatings covered with deposits in simulated air-fired combustion gases after 1000 h at 650 °C

(Ref 10). The bulk of the pit was composed of chromium and oxygen (chromium oxide). Both sodium and potassium were also detected in the mixed deposit/corrosion product layer.

Figure 6(c) shows the cross section and EDX maps of plasma-sprayed FeCrAl coating following the exposure in the test. Aluminum had migrated to the coating-substrate and coating-mixed deposit/corrosion product boundaries leaving the bulk of the coating depleted in aluminum. The innermost scale on the coating was mainly composed of chromium oxide, below which a band of sulfur was detected. Similarly, plasma-sprayed NiCrAlY also showed the presence of sulfur underneath the scale. Aluminum and oxygen were found in higher concentrations in the outer layer of mixed deposit/corrosion product, and chromium and oxygen were found in higher concentrations in the inner layer of the mixed deposit/corrosion product. Thermodynamically, aluminum oxide is more stable than chromium oxide; however, the test temperature was too low for a protective layer of alumina to form. It has been reported in several studies that, in fireside corrosion tests (also in type II hot corrosion for gas turbines), chromium in the alloy plays a crucial role in providing protection rather than aluminum (Ref 30, 31).

3.3.3 Coating-Environment and Coatings-Substrate Interactions. Figures 7 and 8 show the high magnification BSE images of the top section (coating-deposit/gas interface) of the two best-performing coatings: NiCr and FeCrAl (both HVOF and plasma sprayed) after exposure with deposits in simulated air-fired combustion gases at 650 °C for 1000 h. The microstructures of the HVOF-sprayed NiCr and FeCrAl coatings showed the presence of partially melted particles and layers of oxides surrounding the particles. It can be seen that the corrosion front progressed along the interparticle splats. The presence of intersplat boundaries in thermal-sprayed coatings forms the weakest links and so are the places where corrosion is most likely to start. With the onset of corrosion at the splat boundaries and formation of corrosion product, the interface can develop cracks and blisters (Ref 11). In the presence of interconnected porosity, the molten salt/corrosive gases can percolate through the coating and attack the particle boundaries and coating-substrate interfaces. The higher level of porosity and poor interparticle splat boundaries allowed the corrosion to progress rapidly in the HVOF-sprayed coatings compared with the plasma-sprayed coatings.

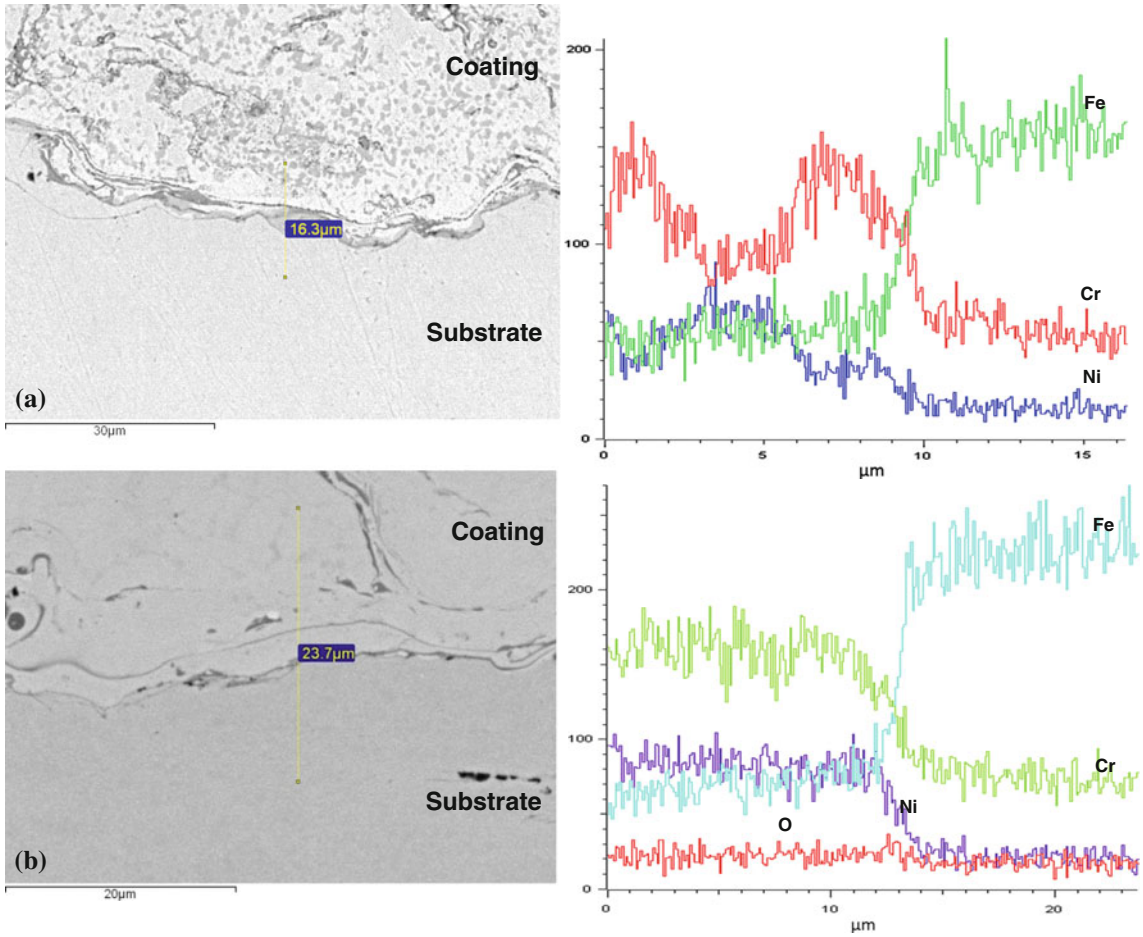

Fig. 9 High magnification BSE images and their corresponding line scans of the coating-substrate interface of HVOF-sprayed (a) NiCr and (b) FeCrAl coatings after exposure in simulated air-fired combustion gases for 1000 h at 650 °C

An additional factor which can lead to enhanced degradation of coatings is the interdiffusion of elements at the coating-substrate interface. This can lead to depletion of important elements, such as Al and Cr from the coating, in addition to the formation of brittle intermetallic phases which can lead to premature coating delamination in service conditions (Ref 30). Figure 9 shows the cross sections of HVOF-sprayed NiCr and FeCrAl coatings on T91 substrates after exposure in the simulated air-fired combustion gases with deposits for 1000 h at 650 °C. The NiCr coating-T91 substrate interface showed a continuous thin band (a mild gray contrast in the BSE image, between the contrast of the coating and the substrate) at the coating side. The line scan showed the phase is rich in chromium. It was not possible to identify the phase reliability using the EDX spot analysis. However, a study by Sundararajan et al. (Ref 32) reported the formation of chromium carbide phase at the interface of Ni:Cr coating-T91 alloy substrate in a steam oxidation test. Figure 9(b) shows the HVOF-sprayed FeCrAl coating-T91 substrate interface following the test. No new phase was observed at the coating-substrate interface. An iron-based coating applied on an iron-based substrate avoided the formation of such a phase; the corresponding line scan showed sharp changes in compositions at the coating-substrate interface.

4. Conclusions

This article reports the results of a series of fireside corrosion tests carried out at 650 °C for 1000 h using the well-established deposit-recoat test method. The test environment was targeted at simulating the corrosive environments on the surfaces of superheaters/reheaters in plants firing a mixture of a coal (UK Daw Mill) and a biomass (CCP) at a ratio of 80:20 (wt.%). Alloy 625, NiCr, FeCrAl, and NiCrAlY feedstock powders were sprayed using HVOF-spraying equipment and plasma-spraying equipment onto a ferritic steel (T91). Dimensional metrology was used as the primary route for quantifying the damage of the coatings.

Deposit D1, simulating alkali-iron tri-sulfate, was found to be very aggressive to all four coatings in the simulated air-fired combustion gases. NiCr was found to be the best-performing coating with a median metal loss of

~87 μm (HVOF sprayed) and ~13 μm (plasma sprayed). In general, the median metal damage for coatings had the following ranking (in the descending order from the largest to the least damage): NiCrAlY > alloy 625 > FeCrAl > NiCr. This performance is strongly dependent on the amount of chromium in the coating, which can produce a protective chromium oxide layer at the test temperature. The chromium scale was attacked by the deposits and the gases from the combustion stream, and a layer of sulfur was detected underneath the chromium oxide layer. In this study, all four plasma-sprayed coatings performed better than the HVOF-sprayed coatings because of lower levels of porosity and good interparticle bondings. The coating-substrate interfaces were also investigated and a chromium-rich layer was detected at the NiCr coating-T91 substrate interface.

Acknowledgments

The authors acknowledge the supports from the ASPECT project, which is a Technology Strategy Board (TSB)-funded project, and especially thank the following companies: Doosan Babcock, E.ON, the National Physical Laboratory, Sulzer Metco, Monitor Coatings, and RWE npower, for their valuable contributions to the project. The authors would also like to thank Dr Johannes Rauch from Sulzer Metco WOKA GmbH for his kind cooperation during this project.

References

1. J. Skea and P. Ekins, Making the Transition to a Secure and Low-Carbon Energy System, *UKERC Energy 2050 Project*; S3097:30, 2009
2. DTI, Biomass Strategy—Economic Analysis of Biomass Energy, DTI Report URN 07/950, 2007, p 1-70
3. J. Stringer and I.G. Wright, Current Limitations of High-Temperature Alloys in Practical Applications, *Oxid. Met.*, 1995, **44**(1), p 265-308
4. N.J. Simms, Environmental Degradation of Boiler Components, *Power Plant Life Management and Performance Improvement*, J.E. Oakey, Ed., Woodhead Publishing, 2011, p 145-179
5. N.J. Simms, P.J. Kilgallon, and J.E. Oakey, Fireside Issues in Advanced Power Generation Systems, *Energy Mater. Mater. Sci. Eng. Energy Syst.*, 2007, **2**(3), p 154-160
6. N.J. Simms, P.J. Kilgallon, and J.E. Oakley, Degradation of Heat Exchanger Materials Under Biomass Co-firing Conditions, *Mater. High Temp.*, 2007, **24**(4), p 333-342
7. T. Hussain, A.U. Syed, and N.J. Simms, Fireside Corrosion of Superheater Materials in Coal/Biomass Co-fired Advanced Power Plants, *Oxid. Met.*, in press
8. A.U. Syed, T. Hussain, N.J. Simms, and J.E. Oakey, Microscopy of Fireside Corrosion on Superheater Materials for Oxy-Fired Pulverised Fuel Power Plants, *Mater. High Temp.*, 2012, **29**(3), p 219-228
9. A.U. Syed, T. Hussain, J.E. Oakey, and N.J. Simms, Fireside Corrosion of Superheater Materials in Oxy-Fired Power Plants, *Eurocorr* (Stockholm), 2011, p 1062-1078
10. A.U. Syed, N.J. Simms, and J.E. Oakey, Fireside Corrosion of Superheaters: Effects of Air and Oxy-Firing of Coal and Biomass, *Fuel*, 2012, **101**, p 62-73
11. S. Paul and M. Harvey, Corrosion Testing of Ni Alloy HVOF Coatings in High Temperature Environments for Biomass Applications, *J. Therm. Spray Technol.* doi:10.1007/s11666-012-9820-8
12. N. Bala, H. Singh, and S. Prakash, High Temperature Corrosion Behavior of Cold Spray Ni-20Cr Coating on Boiler Steel in Molten Salt Environment at 900 °C, *J. Therm. Spray Technol.*, 2010, **19**(1), p 110-118
13. N. Bala, H. Singh, S. Prakash, and J. Karthikeyan, Investigations on the Behavior of HVOF and Cold Sprayed Ni-20Cr Coating on T22 Boiler Steel in Actual Boiler Environment, *J. Therm. Spray Technol.*, 2012, **21**(1), p 144-158
14. J.R. Davis, *Handbook of Thermal Spray Technology*, TSS/ASM International, Materials Park, OH, 2004
15. D. Zhang, S.J. Harris, and D.G. McCartney, Microstructure Formation and Corrosion Behaviour in HVOF-Sprayed Inconel 625 Coatings, *Mater. Sci. Eng. A*, 2003, **344**(1-2), p 45-56
16. T.S. Sidhu, S. Prakash, and R.D. Agrawal, Studies on the Properties of High-Velocity Oxy-Fuel Thermal Spray Coatings for Higher Temperature Applications, *Mater. Sci.*, 2005, **41**(6), p 805-823
17. H. Edris, D. McCartney, and A. Sturgeon, Microstructural Characterization of High Velocity Oxy-Fuel Sprayed Coatings of Inconel 625, *J. Mater. Sci.*, 1997, **32**(4), p 863-872
18. N.J. Simms and A.T. Fry, Modelling Fireside Corrosion of Heat Exchangers in Co-fired Pulverised Fuel Power Systems, *Materials for Advanced Power Engineering*, J. Lecomte-Beckers and M. Carton, Ed., Forschungszentrum Jülich GmbH, 2010
19. Draft Code of Practice for Discontinuous Corrosion Testing in High Temperature Gaseous Atmospheres, *EC Project SMT3-CT95-2001, TESTCORR*, ERA Technology, UK, 2000
20. Corrosion of Metals and Alloys—Methods for Metallographic Examination of Samples After Exposure to High Temperature Corrosive Environments, *Draft ISO Standard. ISO/TC 156 NWI 5092005*, 2006
21. S.R.J. Saunders, *Guidelines for Methods of Testing and Research in High Temperature Corrosion*, H.J. Grabke and D.B. Meadowcroft, Ed., The Institute of Metals, 1995, p 85
22. K. Natesan and J.H. Park, Fireside and Steamside Corrosion of Alloys for USC Plants, *Int. J. Hydrogen Energy*, 2007, **32**(16), p 3689-3697
23. E. Raask, *Mineral Impurities in Coal Combustion*, Hemisphere Publishing Corporation, Washington, DC, 1985
24. J.R. Nicholls, N.J. Simms, and A. Encinas-Oropesa, Modelling Hot Corrosion in Industrial Gas Turbines, *Mater. High Temp.*, 2007, **24**(3), p 149-192
25. T. Hussain, D.G. McCartney, P.H. Shipway, and T. Marrocco, Corrosion Behavior of Cold Sprayed Titanium Coatings and Free Standing Deposits, *J. Therm. Spray Technol.*, 2011, **20**(1-2), p 260-274
26. V. Higuera, F.J. Belzunce, A. Carriles, and S. Poveda, Influence of the Thermal-Spray Procedure on the Properties of a Nickel-Chromium Coating, *J. Mater. Sci.*, 2002, **37**(3), p 649-654
27. F. Azarmi, T.W. Coyle, and J. Mostaghimi, Optimization of Atmospheric Plasma Spray Process Parameters Using a Design of Experiment for Alloy 625 Coatings, *J. Therm. Spray Technol.*, 2008, **17**(1), p 144-155
28. F.H. Yuan, Z.X. Chen, Z.W. Huang, Z.G. Wang, and S.J. Zhu, Oxidation Behavior of Thermal Barrier Coatings with HVOF and Detonation-Sprayed NiCrAlY Bondcoats, *Corros. Sci.*, 2008, **50**(6), p 1608-1617
29. J.R. Nicholls and P. Hancock, Analysis of Oxidation and Hot Corrosion Data—A Statistical Approach, *International Corrosion Conference Series*, NACE, San Diego, CA, 1983, p 198-210
30. N. Birks and G.H. Meier, *Introduction to High Temperature Oxidation of Metals*, Edward Arnold, London, 1983
31. D. Young, *High Temperature Oxidation and Corrosion of Metals*, Elsevier, Amsterdam, 2008
32. T. Sundararajan, S. Kuroda, and F. Abe, Effect of Thermal Spray on the Microstructure and Adhesive Strength of High-Velocity Oxy-Fuel-Sprayed Ni-Cr Coatings on 9Cr-1Mo Steel, *Metall. Mater. Trans. A*, 2004, **35**(10), p 3187-3199